

ARTICLE

Open Access

# Efficient and stable hybrid perovskite-organic light-emitting diodes with external quantum efficiency exceeding 40 per cent

Lingmei Kong<sup>1</sup>, Yun Luo<sup>1</sup>, Qianqian Wu<sup>1</sup>, Xiangtian Xiao<sup>2</sup>, Yuanzhi Wang<sup>1</sup>, Guo Chen<sup>1</sup>, Jianhua Zhang<sup>1</sup>, Kai Wang<sup>2</sup>, Wallace C. H. Choy<sup>3</sup>, Yong-Biao Zhao<sup>4</sup>, Hongbo Li<sup>5</sup>, Takayuki Chiba<sup>6</sup>, Junji Kido<sup>6</sup> and Xuyong Yang<sup>1</sup>

## Abstract

Light-emitting diodes (LEDs) based on perovskite semiconductor materials with tunable emission wavelength in visible light range as well as narrow linewidth are potential competitors among current light-emitting display technologies, but still suffer from severe instability driven by electric field. Here, we develop a stable, efficient and high-color purity hybrid LED with a tandem structure by combining the perovskite LED and the commercial organic LED technologies to accelerate the practical application of perovskites. Perovskite LED and organic LED with close photoluminescence peak are selected to maximize photon emission without photon reabsorption and to achieve the narrowed emission spectra. By designing an efficient interconnecting layer with p-type interface doping that provides good opto-electric coupling and reduces Joule heating, the resulting green emitting hybrid LED shows a narrow linewidth of around 30 nm, a peak luminance of over 176,000 cd m<sup>-2</sup>, a maximum external quantum efficiency of over 40%, and an operational half-lifetime of over 42,000 h.

## Introduction


Light-emitting diodes (LEDs), one of core parts of display equipment, are required to fulfill the requirements of Rec. 2020 color gamut standard for the next-generation display applications. Metal-halide perovskites have extremely narrowband emissions (full-width-at-half-maximum, FWHM  $\leq$  20 nm) and easily tunable bandgap (emission range: 410–850 nm), which are the only a few kinds of emitters that can fully satisfy the Rec.2020 so far<sup>1–8</sup>. The fast advances in perovskite LEDs (PeLEDs) have been made in the past few years and the current external quantum efficiency (EQEs) of PeLEDs have approached 30%<sup>9–19</sup>, comparable to those of commercial organic LEDs (OLEDs). However, the intrinsic instability

of perovskites still casts a shadow over their practical applications<sup>20–23</sup>.

Combining highly color-purity perovskite emitters with other mature display technologies such as OLEDs to expand the display color gamut could be a shortcut towards commercialization for high-definition displays. Perovskite emitters on the other hand can also be deposited by thermal evaporation in vacuum, which is well compatible with production lines of OLEDs<sup>24–27</sup>. Thus, taking advantage of existing OLED-related equipment and processing, the integration of perovskite and OLED will be a rational solution. Indeed, hybrid display technologies have already developed and may become the mainstream trend for display field in the future. For example, a quantum dot liquid crystal TV is fabricated by applying quantum dot patterned color filters and liquid crystal display<sup>28,29</sup>, and a white light LED is prepared by combining QLEDs with OLEDs<sup>30</sup>. Tandem LEDs that connect two or more electroluminescence (EL) units of LEDs through a unique interconnecting layer (ICL) can offer an effective way to integrate the different technologies for better display applications<sup>31–34</sup>. Another

Correspondence: Jianhua Zhang (jh Zhang@shu.edu.cn) or Kai Wang (wangk@sustech.edu.cn) or Xuyong Yang (yangxy@shu.edu.cn)  
<sup>1</sup>Key Laboratory of Advanced Display and System Applications of Ministry of Education, Shanghai University, Shanghai 200072, China  
<sup>2</sup>Institute of Nanoscience and Applications, Department of Electrical and Electronic Engineering, Southern University of Science and Technology, Shenzhen 518055, China  
Full list of author information is available at the end of the article

© The Author(s) 2024

 **Open Access** This article is licensed under a Creative Commons Attribution 4.0 International License, which permits use, sharing, adaptation, distribution and reproduction in any medium or format, as long as you give appropriate credit to the original author(s) and the source, provide a link to the Creative Commons licence, and indicate if changes were made. The images or other third party material in this article are included in the article's Creative Commons licence, unless indicated otherwise in a credit line to the material. If material is not included in the article's Creative Commons licence and your intended use is not permitted by statutory regulation or exceeds the permitted use, you will need to obtain permission directly from the copyright holder. To view a copy of this licence, visit <http://creativecommons.org/licenses/by/4.0/>.

important advantage of tandem devices is that the operational lifetime can be dramatically improved due to the reduced current under the same luminance, which is especially beneficial for the PeLEDs.

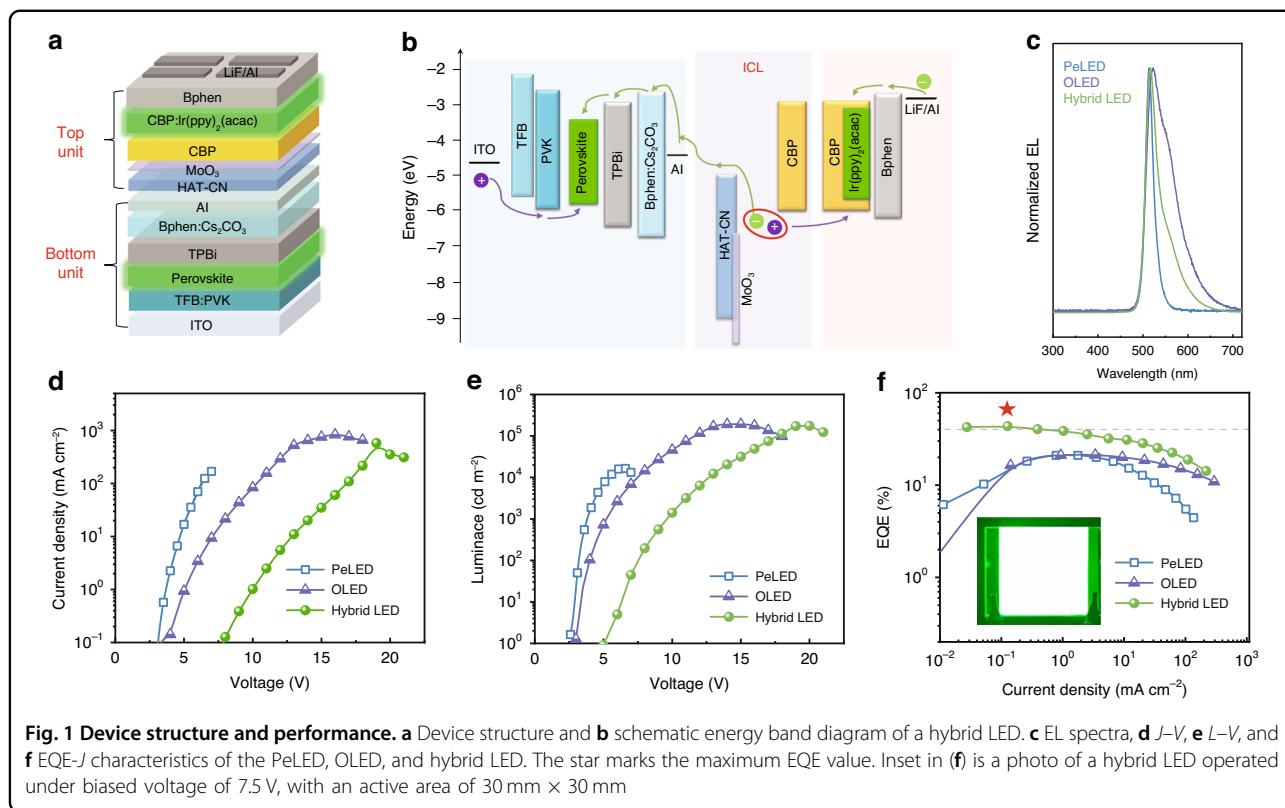
In this work, hybrid perovskite-organic LEDs are proposed to provide an alternative route for accelerating commercialization of perovskite. Specifically, an efficient ICL consisting of 1,4,5,8,9,11-hexaazatriphenylene hexacarbonitrile (HAT-CN)/MoO<sub>3</sub>/(4,4'-bis(N-carbazolyl)-1,1'-biphenyl) (CBP) is demonstrated to show high transmittance and good electrical connection. And by combining with good light-coupling design, green emitting PeLED and OLED with similar photoluminescence (PL) peak are well connected, achieving remarkable device performance. Benefiting from the high color purity of PeLED, the emission linewidth of the hybrid LEDs can be effectively tuned and a narrow FWHM of only around 30 nm is obtained in the optimized devices. Meanwhile, the resulting LEDs also demonstrate high electroluminescence (EL) performance, with a peak EQE of 43.42%, a maximum luminance of 176,166 cd m<sup>-2</sup>, and a long half-lifetime of 42,080 h at an initial luminance of 100 cd m<sup>-2</sup>.

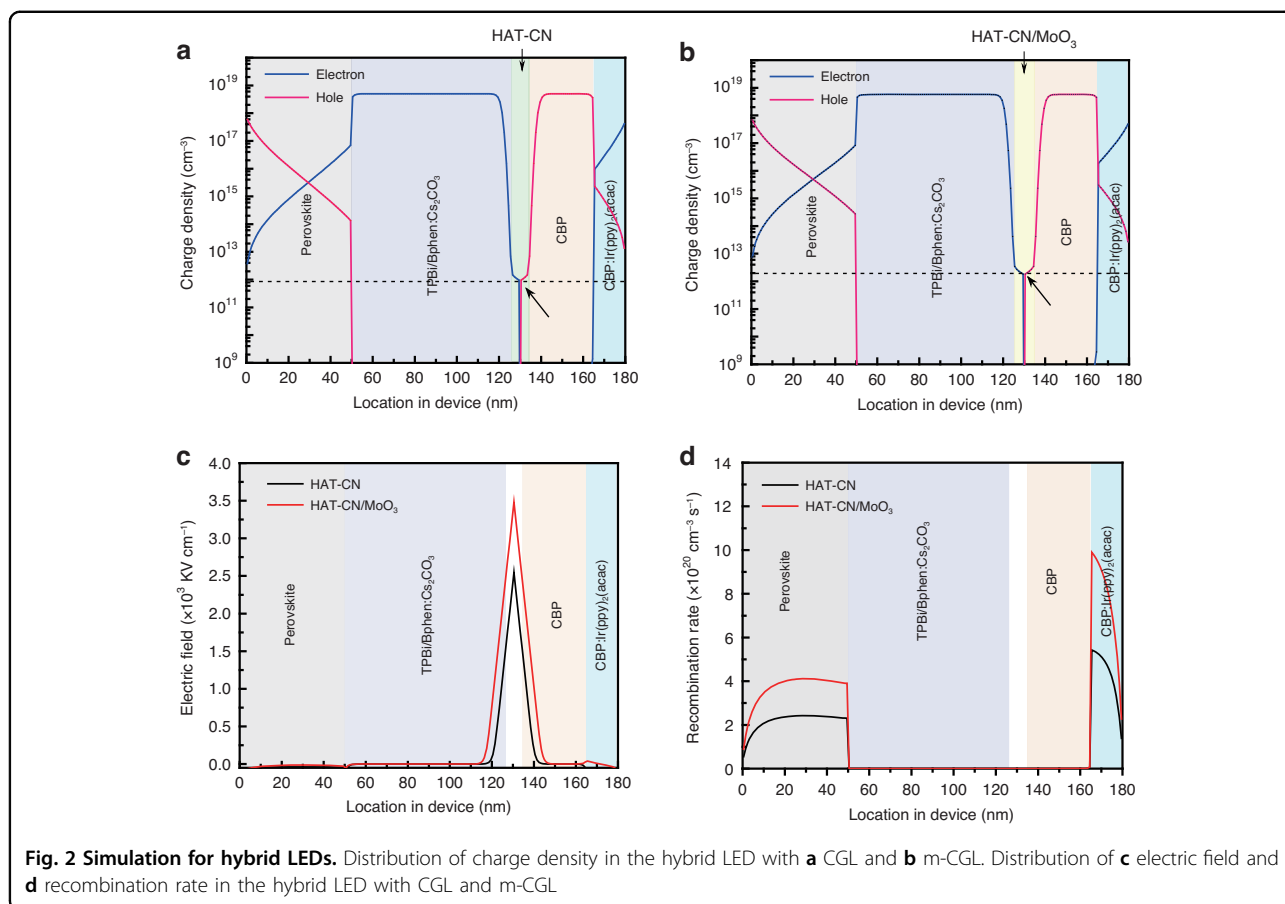
## Results

The hybrid LED consists of a bottom PeLED and a top CBP:Ir(ppy)<sub>2</sub>(acac)-based OLED (Fig. 1a), which are

vertically stacked and connected through an ICL that consists of HAT-CN as electron generation/separation layer, CBP as hole generation/separation layer, and MoO<sub>3</sub> as the charge enhancement layer between HAT-CN and CBP. The energy band diagram of the hybrid device is shown in Fig. 1b, and the corresponding energy level values are from reported works<sup>35</sup>. As schematically illustrated, carriers are expected to efficiently generate at the interface of MoO<sub>3</sub> and CBP as a result of the well-aligned energy levels of the proposed ICL and inject into the bottom PeLED and the top OLED under forward bias<sup>36</sup>. Note that the thicknesses for both the Al and MoO<sub>3</sub> layers within devices are very thin. Unlike external Al electrode, the thin Al layer facilitates the electron separation and transport from the ICL. The ultra-thin MoO<sub>3</sub> (only ~1 nm) allows holes to tunnel through the spacer, which plays an important role in increasing the concentration of charge carriers and extracting the more carriers. MoO<sub>3</sub> has a deeper unoccupied lowest molecular orbital (LUMO) than that of HAT-CN, and meanwhile its LUMO is below the highest occupied molecular orbital (HOMO) of CBP that facilitates electron flow from p-type interface doped CBP to HAT-CN, thereby strengthening the built-in electric field and allowing us to obtain the high-performance devices.

The bottom PeLED with a structure of indium tin oxide (ITO)/poly(9,9-dioctyl-fluorene-co-N-(4-butylphenyl)

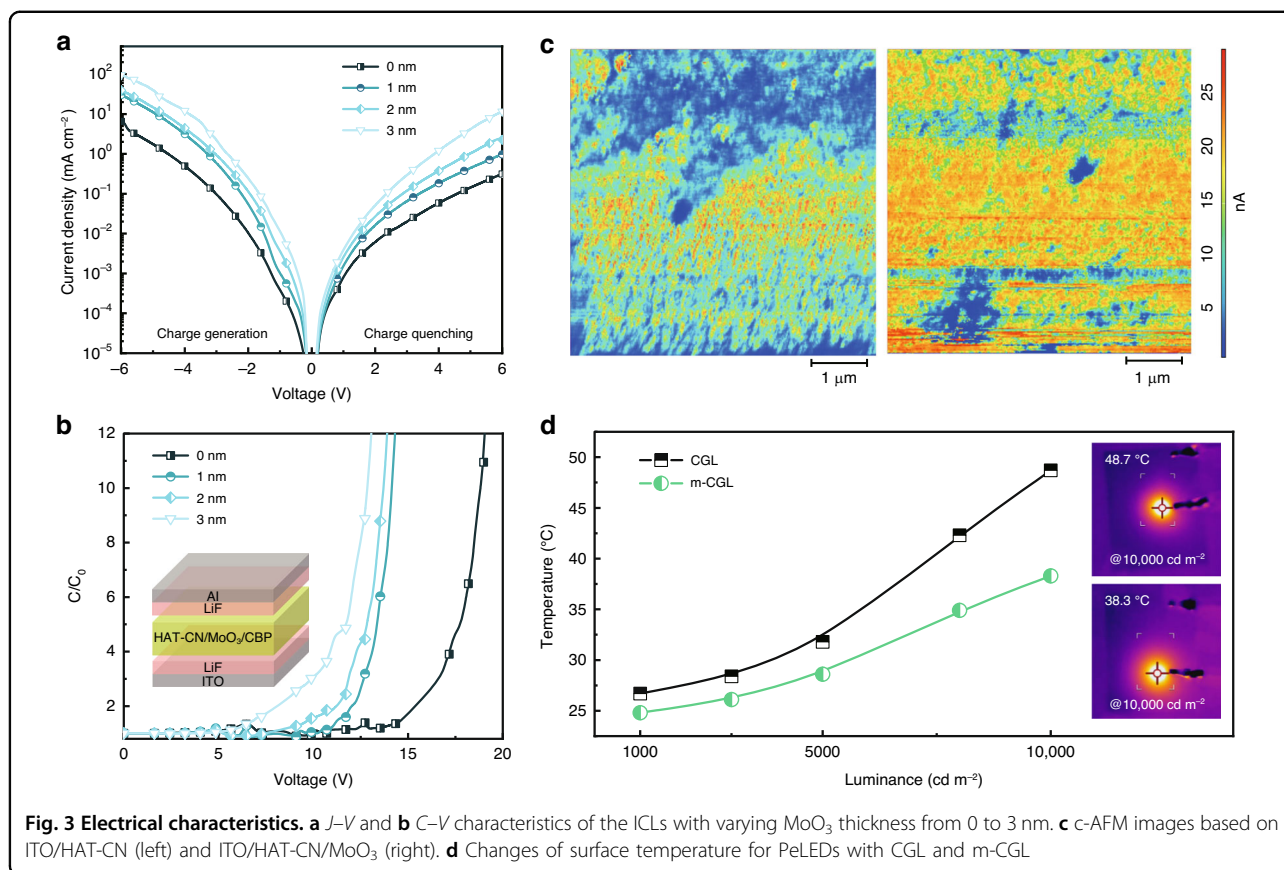




diphenylamine) (TFB): poly(*N*-vinylcarbazole) (PVK)/perovskite/1,3,5-tris(1-phenyl-1H-benzimidazol-2-yl)benzene (TPBi)/4,7-diphenyl-1,10-phenanthroline (Bphen):Cs<sub>2</sub>CO<sub>3</sub>/Al and the top OLED with a structure of ITO/HAT-CN/MoO<sub>3</sub>/CBP/CBP:Ir(ppy)<sub>3</sub>(acac)/TPBi/LiF/Al were also fabricated for comparison. Figure 1c shows the normalized EL spectra of PeLED, OLED, and hybrid LED. The EL peaks of PeLED and OLED are around 514 nm and 523 nm, respectively, while the hybrid LED exhibits a peak centered at 516 nm dominated by the sharp emission linewidth of perovskite emission. Benefiting from the narrow EL emission profile, the hybrid LED shows a FWHM of only 31 nm, which is even less than half that of the OLED (67 nm), indicating its high color-purity. The performance of these proposed LEDs is displayed in Fig. 1d–f. The current density–voltage (*J*–*V*) and luminance–voltage (*L*–*V*) characteristics of the hybrid LED shows slow current injection as a result of a larger resistance induced by the multiple layers, and the luminance reaches 176,166 cd m<sup>-2</sup>, which is much higher than that of the single sub-unit devices (Fig. 1d, e). Notably, a very high peak EQE of 43.42% corresponding to a current efficiency (CE) of 156 cd A<sup>-1</sup> (Fig. S1), almost the sum value of those of PeLED (21.07%) and OLED (21.33%), is obtained,

suggesting the highly-efficient carrier generation, injection and recombination in the hybrid LEDs (Fig. 1f). The detailed EL performances are summarized in Table S1. The inset shows the bright green emission of hybrid LED devices at 7.5 V bias, with a large active area of 30 mm × 30 mm, demonstrating the great potential in large-area display application.

The performance of the hybrid device is closely related to the intermediate connector that should efficiently generate charges at its interface and smoothly inject charges into each sub-unit. To evaluate the optical and electrical properties of the proposed ICL, we investigated two ICLs with structures of HAT-CN/CBP and HAT-CN/MoO<sub>3</sub> (1 nm)/CBP, which are denoted as the charge generation layer (CGL) and m-CGL, respectively. Theoretical analyses of charge density of the hybrid LEDs with CGL and m-CGL were conducted through simulation and calculations, where a well-established physical drift-diffusion model that consists of the continuity equation for electrons and holes coupled with the Poisson equation was used. Furthermore, field-dependent Miller-Abrahams theory was also considered to study the carrier transfer process between Bphen:Cs<sub>2</sub>CO<sub>3</sub>, CGL (or m-CGL) and CBP interfaces<sup>37</sup>. Figure 2a, b shows the distributions of



charge density in the operating LEDs. For the hybrid LED with CGL, the charge densities of separated electrons and holes in HAT-CN/CBP are  $9.53 \times 10^{11} \text{ cm}^{-3}$ , respectively. While in the hybrid LED with m-CGL, 1.9 times increase of the charge density ( $1.83 \times 10^{12} \text{ cm}^{-3}$ ) is obtained at the interface of HAT-CN/ $\text{MoO}_3$ /CBP, indicating a stronger generation and separation rate. The distribution of electric field was further analyzed in Fig. 2c. Due to the efficient charge carrier generation at HAT-CN/CBP interface as described above, electrons and holes are separated to form electric dipoles, thus yielding a build-in electric field. With the insertion of the ultra-thin  $\text{MoO}_3$ , the separation of carriers is promoted, and the number of electric dipoles increases, leading to a notably enhanced electric field. We then present the distribution of the recombination rate in sub-units without/with  $\text{MoO}_3$ . As shown in Fig. 2d, the recombination peaks are observed in both the perovskite and organic emitter layers, and it can be noted that the radiative recombination rate in whether perovskite or organic emitter can be significantly enhanced by 1.8 times when the ultra-thin  $\text{MoO}_3$  is deposited on HAT-CN. These simulation results indicate that the  $\text{MoO}_3$  layer facilitates charge carrier generation and separation from the ICL interface, and then transport smoothly via respective charge transport layers to make efficient

exciton recombine in sub-units. We thus proposed that the charge generation capability can be strengthened when a  $\text{MoO}_3$  layer, with a deeper LUMO than that of HAT-CN, is introduced to HAT-CN/CBP interface. In this case, more electrons transferred from CBP to HAT-CN due to the existence of ultra-thin  $\text{MoO}_3$ , and the hole concentration is increased in CBP, leading to higher hole current. Consequently, electrons and holes are injected into bottom PeLED and top OLED units, resulting in improved radiative recombination.

To investigate the effects of different thicknesses of  $\text{MoO}_3$  in the proposed ICL on the charge generation capability, the  $J$ - $V$  curves of the ICL devices with a structure of ITO/HAT-CN/ $\text{MoO}_3$ /CBP/Al as a function of  $\text{MoO}_3$  thickness varying from 0 to 3 nm were characterized. Under reverse bias, charge carriers are generated at the interface of HAT-CN/CBP and ultimately are extracted by the electrodes, whereas the charge carriers are injected from the electrodes and finally are quenched by the ICL under forward bias. If charge generation and charge quenching are identical, the ICL could generate charges efficiently in balanced fashion<sup>38</sup>. As shown in Fig. 3a, the symmetrical characteristics of  $J$ - $V$  curves of the ICL devices are improved after inserting the thin  $\text{MoO}_3$ , and the current density is continuously increased

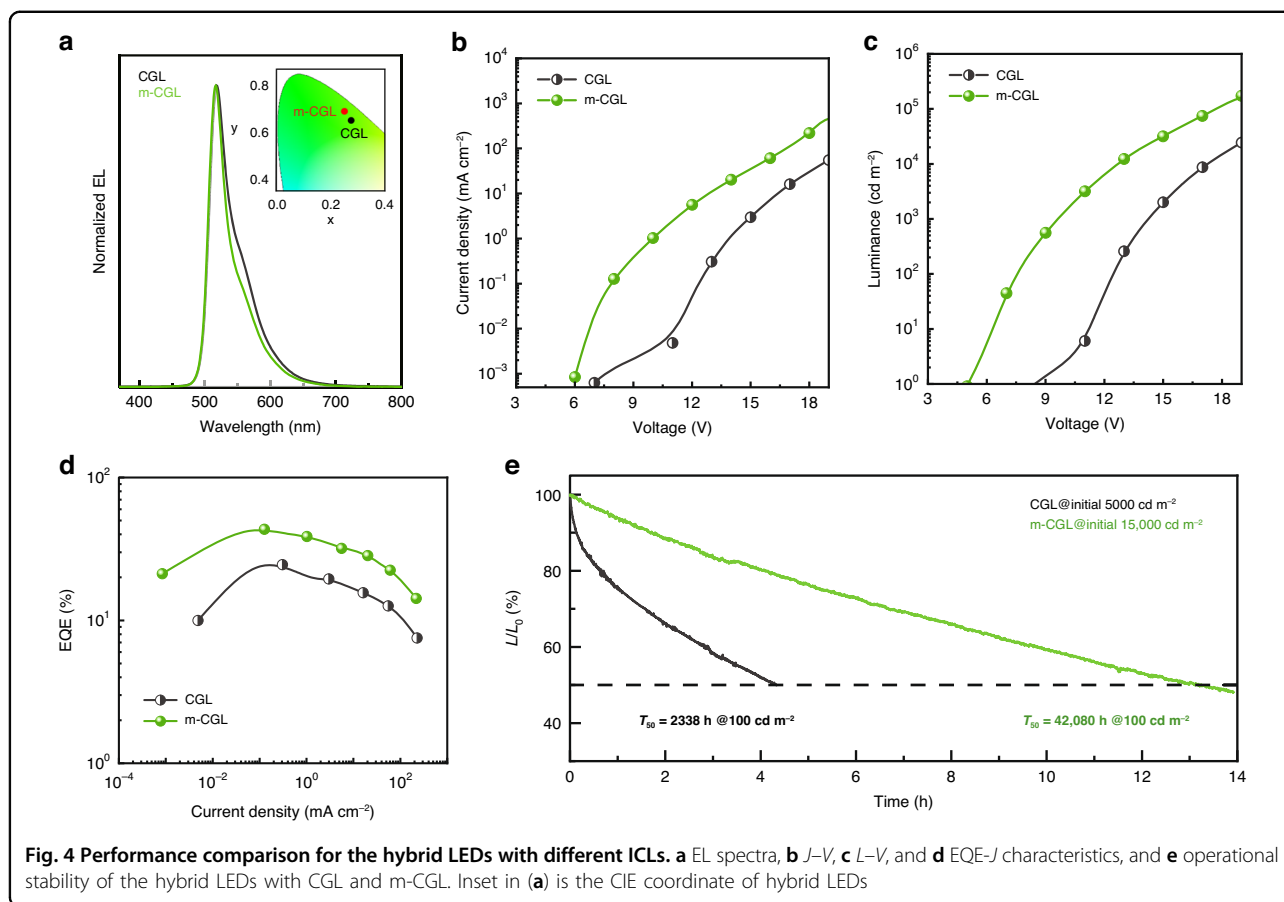


with increasing the thickness of  $\text{MoO}_3$ , indicating that the charge generation and transport capacity are significantly enhanced. Moreover, the capacitance–voltage ( $C$ – $V$ ) characteristics of ICL devices were measured at a fixed frequency of 1 kHz. The device structure was shown in Fig. 3b, in which the double-insulating layers of LiF were introduced to inhibit the injection of charges from the external electrodes. The measured capacitance is normalized by the zero-bias capacitance ( $C_0$ ). The capacitance of the device without  $\text{MoO}_3$  show almost no change before an applied bias of 15 V, suggesting that a larger voltage is needed for the ICL to generate charge. In sharp contrast, for the m-CGL device the voltage required to generate charge is significantly reduced (7 V in 3 nm- $\text{MoO}_3$  devices). Moreover, the ICL with a thicker  $\text{MoO}_3$  layer presents a superior electrical property in comparison to the one with a thinner  $\text{MoO}_3$  layer, consistent with the results of  $J$ – $V$  measurements. The hybrid LEDs with different thicknesses of  $\text{MoO}_3$  were also fabricated and compared (Fig. S2 and Table S2). We found that the EL efficiency reaches the peak value when the thickness of  $\text{MoO}_3$  is at 1 nm and after that the EQE would gradually decreases. The efficiency decline is attributed to a decrease in transmittance of ICL that is detrimental to light outcoupling (Fig. S3) and a sharp increase in current density which can induce performance degradation due to exciton dissociation, Coulombic degradation and/or excessive heating<sup>38</sup>.

In order to clarify the effects of ultra-thin  $\text{MoO}_3$  on the electrical properties of ICL, the morphologies and conductivity of the HAT-CN films without/with  $\text{MoO}_3$  were investigated by atomic force microscopy (AFM) and conductive AFM (c-AFM). We noted that the HAT-CN films without and with depositing  $\text{MoO}_3$  have a similar roughness (Fig. S4), indicating that the surface morphology of the underlying HAT-CN is almost not affected by the ultra-thin layer of  $\text{MoO}_3$ . However, this enables an enhancement in the electrical conductivity of HAT-CN, as revealed by c-AFM (Fig. 3c). From the line profiles of current (Fig. S5), we observed that the bottom of current profile is increased from 2 nA to 8 nA after the deposition of  $\text{MoO}_3$  on HAT-CN. X-ray photoelectron spectra (XPS) shows that  $\text{MoO}_3$  can partially diffused into the HAT-CN film (Fig. S6), thus improve electrical conductivity, which facilitates charge carrier transport of the ICL and suppresses undesired Joule heating due to the decreased resistance. As well known, Joule heating damages the operating stability of the device. We performed surface temperature tests on hybrid devices with CGL and m-CGL operating at different luminance (Fig. S7), and the temperature variation curves are shown in Fig. 3d. Both the devices show a comparable temperature of around 25 °C under a relatively low luminance of 1000  $\text{cd m}^{-2}$ . With the increase of applied voltage, the temperature

difference between the two devices under the same luminance dramatically increases. Especially, the temperature of hybrid LEDs with CGL is 48.7 °C at 10,000  $\text{cd m}^{-2}$ , which is almost 1.3 times higher than that of hybrid LEDs with m-CGL (38.3 °C) at the same luminance. According to the rising trend of temperature, it can be predicted that the hybrid LEDs with m-CGL have a much lower surface temperature even at higher luminance. In addition to reducing heat in devices, the efficient charge transport and injection generated by the m-CGL greatly enhances the luminance. It is worth pointing out that achieving high luminance and efficiency at a low current density accompanied with low heat, is beneficial to long-term operational LEDs.

The EL performance of hybrid LEDs based on CGL and m-CGL is then studied systematically (Fig. 4 and Table S3). Compared to the relatively wide EL FWHM (42 nm) of the LED with CGL, the FWHM of the device with m-CGL is dramatically reduced to 31 nm, and the Commission International de l'Eclairage (CIE) coordinates are accordingly changed from (0.28, 0.64) to (0.25, 0.67) that is closer to pure green light of (0.21, 0.71). The device with m-CGL exhibits faster current injection and higher current density characteristics, due to more efficient charge generation capability of ICL resulting from enhanced electron transfer at the HAT-CN/CBP interface, which is also evidenced by almost no obvious performance difference in the top OLED devices (Fig. S8 and Table S4). With the implementation of m-CGL, the EL performance of device is significantly improved: the luminance and the EQE are increased from 94,633  $\text{cd m}^{-2}$  to over 176,000  $\text{cd m}^{-2}$  and from 25.12% to over 43%, while the  $V_{\text{on}}$  is decreased from 8.5 to 5 V (Fig. 4d, e). The statistical histogram of the max. EQE values shows the average max. EQE values for these devices with CGL and m-CGL are  $22.8 \pm 5.5\%$  and  $39.9 \pm 4.9\%$ , respectively (Fig. S9), demonstrating good device-to-device reproducibility. It is noteworthy that the PeLEDs based on the perovskites with different systems show good compatibility with OLEDs in the hybrid device structures. We tested the operational stability of the hybrid LEDs based on quasi-2D/3D PeLED and OLED in the glove box without any encapsulation. The quasi-2D PeLED and OLED based hybrid LEDs with m-CGL show a half-lifetime ( $T_{50}$ ) of 13.2 h at an initial luminance ( $L_0$ ) of 15,000  $\text{cd m}^{-2}$ , while a 4.3 h  $T_{50}$  for the device with CGL at  $L_0$  of 5000  $\text{cd m}^{-2}$  (Fig. 4e). By using the accelerated lifetime equation ( $L_0^n T_{50} = \text{constant}$ , where  $n$  is an acceleration factor)<sup>39</sup> with  $n = 1.61$  (Fig. S10), we therefore estimated the  $T_{50}$  of the hybrid LEDs with m-CGL at 100  $\text{cd m}^{-2}$  to be 42,080 h, 18-fold improvement than that of the device with CGL. We also noted slight changes in EL spectra after the lifetime test or operated under different applied voltages (Fig. S11), which are ascribe to the



relative instability of PeLEDs. Similarly, the hybrid LEDs with the combination of 3D PeLED and OLED shows significant stability improvement compared with the PeLED-only device, with a long  $T_{50}$  of 78,362 h (Figs. S12 and S13), demonstrating the potential of this hybrid structure on device performance.

## Discussion

In summary, we demonstrated highly efficient and stable hybrid LEDs with remarkable narrow linewidth emission constructed with a top OLED and a bottom PeLED by employing an efficient ICL based on a structure of HAT-CN/MoO<sub>3</sub>/CBP, in which the ultra-thin MoO<sub>3</sub> sandwiched in the organic hole inject layer and hole transport layer not only facilitates the electron transfer from CBP to HAT-CN leaving a p-type doped HTL interface that leads to significant enhancement in the capacity for charge generation, separation and transport of the ICL, but also effectively suppresses the undesired Joule heating due to the decreased resistance. Benefiting from the proposed ICL and combining with good light outcoupling design, the hybrid LED exhibits high color purity, excellent device performance as well as significantly improved stability, representing one of the best

performing tandem LEDs with ultra-high color purity to date. This work shows a great potential in the combination of the two or more display technologies for the practical applications, and the LEDs with high color purity, extremely high efficiency, and long operational lifetime would be ideal candidates to the next generation of full color displays and solid-state lighting markets.

## Materials and methods

### Materials

CsBr (99.999%, metal basis) and PbBr<sub>2</sub> (99.999%, metal basis) were purchased from Alfa Aesar. Phenethylammonium bromide (PEABr) and PEDOT:PSS (Clevious PVP AI 4083) were purchased from Xian Yuri Solar Co, Ltd. PVK and dimethyl sulfoxide (DMSO) (99.9%) were purchased from Sigma-Aldrich. Cs<sub>2</sub>CO<sub>3</sub>, MoO<sub>3</sub>, TFB, Bphen, HAT-CN, CBP, Ir(ppy)<sub>2</sub>(acac), TPBi and LiF were purchased from Luminescence Technology Corp. All of the reagents were directly used as received.

### Preparation of perovskite films

The perovskite precursor solutions were prepared as previous reported with a modification<sup>22,40</sup>. Briefly, quasi-2D perovskite precursor was prepared by dissolving

PbBr<sub>2</sub>, CsBr, and PEABr in anhydrous DMSO with the molar ratio of 1:1.2:0.4. 3D perovskite precursor was obtained by dissolving PbBr<sub>2</sub>, CsBr, and cesium trifluoroacetate in DMSO with the molar ratio of 1:1:0.7. The mixture was stirred at 60 °C for 3 h and filtered through a 0.45 μm polytetrafluoroethylene membrane before use. Perovskite films were deposited on glass or ITO substrates by spin-coating the precursor solutions at 4000 r.p.m for 40 s and annealing at 80 °C for 10 min.

### Device fabrication

TFB:PVK was deposited from its chlorobenzene solution (a weight ratio of 4:6, 10 mg mL<sup>-1</sup>) on the oxygen plasma treated ITO substrates at a speed of 4000 r.p.m. for 40 s, and baked at 120 °C for 20 min. For 3D PeLED, PEDOT:PSS as hole transport layer was spin-coated on the ITO substrates at 4000 rpm for 40 s and then baked at 150 °C for 20 min in air. After the deposition of the perovskite films, the samples were transferred into a high-vacuum deposition system (~4 × 10<sup>-4</sup> Pa) for the successive thermal evaporation of TPBi (40 nm), Bphen:Cs<sub>2</sub>CO<sub>3</sub> (10 wt%, 40 nm), Al (1 nm), HAT-CN (10 nm), MoO<sub>3</sub> (1 nm), CBP (35 nm), CBP:Ir(ppy)<sub>2</sub>(acac) (8 wt%, 15 nm), Bphen (65 nm), LiF (1 nm), and Al (100 nm).

### Device characterizations

Absorption spectra were recorded by using a PerkinElmer Lambda 950 UV-vis-NIR spectrometer. The surface temperature was measured by a FLIR T630sc thermal infrared imager. The *J*-*V* and *C*-*V* curves of the ICL devices were measured by using TTP4 cryogenic probe station. The *J*-*V* and *L*-*V* characteristics of LED devices were collected by using a QE Pro spectrometer and the Keithley 2400 source meter. The LED was tested on top of the integrating sphere, which has been accurately calibrated by a commercially standard LED. The operational lifetime tests of LEDs were performed on a commercialized ZJZCL-1 OLED ageing lifespan test system in a nitrogen-filled glovebox at room temperature. The electroluminescence performance for all the LED devices is measured based on an emission area of 2 mm × 2 mm.

### Simulation

Charge density, electric field, and recombination rate of proposed devices were simulated and quantitatively investigated by SETFOS 4.6, which was already successfully used to characterize organic solar cells<sup>41,42</sup> and LEDs<sup>43,44</sup>. Here the well-established physical drift-diffusion model was used, which is consisted of the continuity equation for electrons and holes coupled with the Poisson equation. Furthermore, electron transfer process between HOMO and deep LUMO (e.g., electron transfer from the HOMO level of BCP to the LUMO of HAT-CN

and MoO<sub>3</sub>) also considered to investigate carrier hopping process in devices. In addition, TPBi and Bphen:Cs<sub>2</sub>CO<sub>3</sub> have been regarded as one “TPBi/Bphen:Cs<sub>2</sub>CO<sub>3</sub>” layer due to their approximate electron mobility and low energy barrier.

### Acknowledgements

We acknowledge financial support from the National Key Research and Development Program of China (2022YFE0200200 and 2022YFB3606504), National Natural Science Foundation of China (62174104 and 62122034), and Program of Shanghai Academic/Technology Research Leader (22XD1421200). G.C. also thanks financial support from Shanghai S&T Committee Project 20392001100.

### Author details

<sup>1</sup>Key Laboratory of Advanced Display and System Applications of Ministry of Education, Shanghai University, Shanghai 200072, China. <sup>2</sup>Institute of Nanoscience and Applications, Department of Electrical and Electronic Engineering, Southern University of Science and Technology, Shenzhen 518055, China. <sup>3</sup>Department of Electrical and Electronic Engineering, The University of Hong Kong, Hong Kong, China. <sup>4</sup>Department of Physics and Lakeside AR/VR Laboratory, International Joint Research Center for Optoelectronic and Engineering Research, Yunnan University, Kunming 650091, China. <sup>5</sup>Experimental Center of Advanced Materials, School of Materials Science and Engineering, Beijing Institute of Technology, Beijing 100081, China. <sup>6</sup>Graduate School of Organic Materials Science, Frontier Center for Organic Materials, Yamagata University, 4-3-16 Jonan, Yonezawa 992-8510, Japan

### Author contributions

X.Y. designed and guided the study. L.K. and Y.L. contributed to experimental work for fabricating and characterizing the LED devices. T.X. and K.W. performed the simulation and calculations. Q.W., Y.W., W.C.H.C., Y.-B.Z., G.C., J.Z., T.C., and J.K. helped to analyze the experimental results. All authors read and commented on the paper.

### Conflict of interest

The authors declare no competing interests.

**Supplementary information** The online version contains supplementary material available at <https://doi.org/10.1038/s41377-024-01500-7>.

Received: 3 December 2023 Revised: 19 May 2024 Accepted: 30 May 2024  
Published online: 12 June 2024

### References

- Kovalenko, M. V., Protesescu, L. & Bodnarchuk, M. I. Properties and potential optoelectronic applications of lead halide perovskite nanocrystals. *Science* **358**, 745–750 (2017).
- Lu, M. et al. Metal halide perovskite light-emitting devices: promising technology for next-generation displays. *Adv. Funct. Mater.* **29**, 1902008 (2019).
- Han, T. H. et al. A roadmap for the commercialization of perovskite light emitters. *Nat. Rev. Mater.* **7**, 757–777 (2022).
- Wang, H. R. et al. A multi-functional molecular modifier enabling efficient large-area perovskite light-emitting diodes. *Joule* **4**, 1977–1987 (2020).
- Jiang, Y. Z. et al. Synthesis-on-substrate of quantum dot solids. *Nature* **612**, 679–684 (2022).
- Wang, C. H. et al. Dimension control of in situ fabricated CsPbClBr<sub>2</sub> nanocrystal films toward efficient blue light-emitting diodes. *Nat. Commun.* **11**, 6428 (2020).
- Song, Y. H. et al. Planar defect-free pure red perovskite light-emitting diodes via metastable phase crystallization. *Sci. Adv.* **8**, eabq2321 (2022).
- Cho, H. et al. Overcoming the electroluminescence efficiency limitations of perovskite light-emitting diodes. *Science* **350**, 1222–1225 (2015).
- Lin, K. B. et al. Perovskite light-emitting diodes with external quantum efficiency exceeding 20 per cent. *Nature* **562**, 245–248 (2018).

10. Hassan, Y. et al. Ligand-engineered bandgap stability in mixed-halide perovskite LEDs. *Nature* **591**, 72–77 (2021).
11. Ma, D. X. et al. Distribution control enables efficient reduced-dimensional perovskite LEDs. *Nature* **599**, 594–598 (2021).
12. Wang, Y. K. et al. In situ inorganic ligand replenishment enables bandgap stability in mixed-halide perovskite quantum dot solids. *Adv. Mater.* **34**, 2200854 (2022).
13. Cao, Y. et al. Perovskite light-emitting diodes based on spontaneously formed submicrometre-scale structures. *Nature* **562**, 249–253 (2018).
14. Liu, Z. et al. Perovskite light-emitting diodes with EQE exceeding 28% through a synergetic dual-additive strategy for defect passivation and nanostructure regulation. *Adv. Mater.* **33**, 2103268 (2021).
15. Chen, Z. M. et al. Utilization of trapped optical modes for white perovskite light-emitting diodes with efficiency over 12%. *Joule* **5**, 456–466 (2021).
16. Liu, Y. J. et al. Synergistic passivation and stepped-dimensional perovskite analogs enable high-efficiency near-infrared light-emitting diodes. *Nat. Commun.* **13**, 7425 (2022).
17. Jiang, J. et al. Red perovskite light-emitting diodes with efficiency exceeding 25% realized by co-spacer cations. *Adv. Mater.* **34**, 2204460 (2022).
18. Han, D. Y. et al. Tautomeric mixture coordination enables efficient lead-free perovskite LEDs. *Nature* **622**, 493–498 (2023).
19. Yang, F. et al. Rational adjustment to interfacial interaction with carbonized polymer dots enabling efficient large-area perovskite light-emitting diodes. *Light Sci. Appl.* **12**, 119 (2023).
20. Guo, B. B. et al. Ultrastable near-infrared perovskite light-emitting diodes. *Nat. Photonics* **16**, 637–643 (2022).
21. Liu, Y. et al. Bright and stable light-emitting diodes based on perovskite quantum dots in perovskite matrix. *J. Am. Chem. Soc.* **143**, 15606–15615 (2021).
22. Wang, H. R. et al. Trifluoroacetate induced small-grained CsPbBr<sub>3</sub> perovskite films result in efficient and stable light-emitting devices. *Nat. Commun.* **10**, 665 (2019).
23. Chen, W. J. et al. Highly bright and stable single-crystal perovskite light-emitting diodes. *Nat. Photon.* **17**, 401–407 (2023).
24. Du, P. P. et al. Efficient and large-area all vacuum-deposited perovskite light-emitting diodes via spatial confinement. *Nat. Commun.* **12**, 4751 (2021).
25. Fu, Y. et al. Scalable all-evaporation fabrication of efficient light-emitting diodes with hybrid 2D–3D perovskite nanostructures. *Adv. Funct. Mater.* **30**, 2002913 (2020).
26. Du, P. P. et al. Vacuum-deposited blue inorganic perovskite light-emitting diodes. *ACS Appl. Mater. Interfaces* **11**, 47083–47090 (2019).
27. Yang, X. Y. et al. Focus on perovskite emitters in blue light-emitting diodes. *Light Sci. Appl.* **12**, 177 (2023).
28. Ko, Y. H. et al. Super ultra-high resolution liquid-crystal-display using perovskite quantum-dot functional color-filters. *Sci. Rep.* **8**, 12881 (2018).
29. Ko, Y. H. et al. Environmentally friendly quantum-dot color filters for ultra-high-definition liquid crystal displays. *Sci. Rep.* **10**, 15817 (2020).
30. Zhang, H., Su, Q. & Chen, S. M. Quantum-dot and organic hybrid tandem light-emitting diodes with multi-functionality of full-color-tunability and white-light-emission. *Nat. Commun.* **11**, 2826 (2020).
31. Wang, R. et al. Minimizing energy barrier in intermediate connection layer for monolithic tandem WPeLEDs with wide color gamut. *Adv. Funct. Mater.* **33**, 2215189 (2023).
32. Jia, Z. R. et al. Near-infrared absorbing acceptor with suppressed triplet exciton generation enabling high performance tandem organic solar cells. *Nat. Commun.* **14**, 1236 (2023).
33. Lee, H. D. et al. Valley-centre tandem perovskite light-emitting diodes. *Nat. Nanotechnol.* **19**, 624–631 (2024).
34. Sun, S. Q. et al. Highly efficient hybrid perovskite/organic tandem white light emitting-diodes with external quantum efficiency exceeding 20. *Adv. Funct. Mater.* **33**, 2306549 (2023).
35. Helander, M. G. et al. Chlorinated indium tin oxide electrodes with high work function for organic device compatibility. *Science* **332**, 944–947 (2011).
36. Hamwi, S. et al. The role of transition metal oxides in charge-generation layers for stacked organic light-emitting diodes. *Adv. Funct. Mater.* **20**, 1762–1766 (2010).
37. Xiao, X. T. et al. Enhanced hole injection assisted by electric dipoles for efficient perovskite light-emitting diodes. *Commun. Mater.* **1**, 81 (2020).
38. Wu, Q. Q. et al. Efficient tandem quantum-dot LEDs enabled by an inorganic semiconductor-metal-dielectric interconnecting layer stack. *Adv. Mater.* **34**, 2108150 (2022).
39. Woo, S. J., Kim, J. S. & Lee, T. W. Characterization of stability and challenges to improve lifetime in perovskite LEDs. *Nat. Photonics* **15**, 630–634 (2021).
40. Kong, L. M. et al. Smoothing the energy transfer pathway in quasi-2D perovskite films using methanesulfonate leads to highly efficient light-emitting devices. *Nat. Commun.* **12**, 1246 (2021).
41. Neukom, M. T., Reinke, N. A. & Ruhstaller, B. Charge extraction with linearly increasing voltage: a numerical model for parameter extraction. *Sol. Energy* **85**, 1250–1256 (2011).
42. Züfle, S. et al. An effective area approach to model lateral degradation in organic solar cells. *Adv. Energy Mater.* **5**, 1500835 (2015).
43. Altazin, S. et al. Simulation of OLEDs with a polar electron transport layer. *Org. Electron.* **39**, 244–249 (2016).
44. Ruhstaller, B. et al. In *Optoelectronic Devices and Properties* (ed. Sergiyenko, O.) (Intechopen, 2011).